A&A 671, A12 (2023)
https://doi.org/10.1051/0004-6361/202244931

Astronomy & Astrophysics

MAGIC observations provide compelling evidence of hadronic multi-TeV emission from the putative PeVatron SNR G106.3+2.7

MAGIC Collaboration: H. Abe[1], S. Abe[1], V. A. Acciari[2], I. Agudo[3], T. Aniello[4], S. Ansoldi[5,45], L. A. Antonelli[4], A. Arbet Engels[6], C. Arcaro[7], M. Artero[8], K. Asano[1], D. Baack[9], A. Babić[10], A. Baquero[11], U. Barres de Almeida[12], J. A. Barrio[11], I. Batković[7], J. Baxter[1], J. Becerra González[2], W. Bednarek[13], E. Bernardini[7], M. Bernardos[3], A. Berti[6], J. Besenrieder[6], W. Bhattacharyya[14], C. Bigongiari[4], A. Biland[15], O. Blanch[8], G. Bonnoli[4], Ž. Bošnjak[10], I. Burelli[5], G. Busetto[7], R. Carosi[16], M. Carretero-Castrillo[17], A. J. Castro-Tirado[3], G. Ceribella[1], Y. Chai[6], A. Chilingarian[18], S. Cikota[10], E. Colombo[2], J. L. Contreras[11], J. Cortina[19], S. Covino[4], G. D'Amico[20], V. D'Elia[4], P. Da Vela[4,16], F. Dazzi[4], A. De Angelis[7], B. De Lotto[5], A. Del Popolo[21], M. Delfino[8,47], J. Delgado[8,47], C. Delgado Mendez[19], D. Depaoli[22], F. Di Pierro[22], L. Di Venere[23], E. Do Souto Espiñeira[8], D. Dominis Prester[24], A. Donini[4], D. Dorner[25], M. Doro[7], D. Elsaesser[9], G. Emery[26], J. Escudero[3], V. Fallah Ramazani[27,48], L. Fariña[8], A. Fattorini[9], L. Font[28], C. Fruck[6], S. Fukami[15], Y. Fukazawa[29], R. J. García López[2], M. Garczarczyk[14], S. Gasparyan[30], M. Gaug[28], J. G. Giesbrecht Paiva[12], N. Giglietto[23], F. Giordano[23], P. Gliwny[13], N. Godinović[31], R. Grau[8], D. Green[6], J. G. Green[6], D. Hadasch[1], A. Hahn[6], T. Hassan[19], L. Heckmann[6,46], J. Herrera[2], D. Hrupec[32], M. Hütten[1], R. Imazawa[29], T. Inada[1], R. Iotov[25], K. Ishio[13], I. Jiménez Martínez[19], J. Jormanainen[27], D. Kerszberg[8], Y. Kobayashi[1], H. Kubo[1], J. Kushida[33], A. Lamastra[4], D. Lelas[31], F. Leone[4], E. Lindfors[27], L. Linhoff[9], S. Lombardi[4], F. Longo[5,50], R. López-Coto[7], M. López-Moya[11], A. López-Oramas[2], S. Loporchio[23], A. Lorini[34], E. Lyard[26], B. Machado de Oliveira Fraga[12], P. Majumdar[35,50], M. Makariev[36], G. Maneva[36], N. Mang[9], M. Manganaro[24], S. Mangano[19], K. Mannheim[25], M. Mariotti[7], M. Martínez[8], A. Mas Aguilar[11], D. Mazin[1,6], S. Menchiari[34], S. Mender[9], S. Mićanović[24], D. Miceli[7], T. Miener[11], J. M. Miranda[34], R. Mirzoyan[6], E. Molina[17], H. A. Mondal[35], A. Moralejo[8], D. Morcuende[11], V. Moreno[28], T. Nakamori[37], C. Nanci[4], L. Nava[4], V. Neustroev[38], M. Nievas Rosillo[2], C. Nigro[8], K. Nilsson[27], K. Nishijima[33], T. Njoh Ekoume[2], K. Noda[1], S. Nozaki[6], Y. Ohtani[1], T. Oka[39,⋆], A. Okumura[40], J. Otero-Santos[2], S. Paiano[4], M. Palatiello[5], D. Paneque[6], R. Paoletti[34], J. M. Paredes[17], L. Pavletić[24], M. Persic[5], M. Pihet[6], G. Pirola[6], F. Podobnik[34], P. G. Prada Moroni[16], E. Prandini[7], G. Principe[5], C. Priyadarshi[8], W. Rhode[9], M. Ribó[17], J. Rico[8], C. Righi[4], A. Rugliancich[16], N. Sahakyan[30], T. Saito[1,⋆], S. Sakurai[1], K. Satalecka[27], F. G. Saturni[4], B. Schleicher[25], K. Schmidt[9], F. Schmuckermaier[6], J. L. Schubert[9], T. Schweizer[6], J. Sitarek[13], V. Sliusar[26], D. Sobczynska[13], A. Spolon[7], A. Stamerra[4], J. Strišković[32], D. Strom[6], M. Strzys[1,⋆], Y. Suda[29], T. Surić[41], H. Tajima[40], M. Takahashi[40], R. Takeishi[1], F. Tavecchio[4], P. Temnikov[36], K. Terauchi[39], T. Terzić[24], M. Teshima[1,6], L. Tosti[42], S. Truzzi[34], A. Tutone[4], S. Ubach[28], J. van Scherpenberg[6], M. Vazquez Acosta[2], S. Ventura[34], V. Verguilov[36], I. Viale[7], C. F. Vigorito[22], V. Vitale[43], I. Vovk[1], R. Walter[26], M. Will[6], C. Wunderlich[34], T. Yamamoto[44], and D. Zarić[31]

(Affiliations can be found after the references)

Received 9 September 2022 / Accepted 11 November 2022

ABSTRACT

Context. Certain types of supernova remnants (SNRs) in our Galaxy are assumed to be PeVatrons, capable of accelerating cosmic rays (CRs) to ∼ PeV energies. However, conclusive observational evidence for this has not yet been found. The SNR G106.3+2.7, detected at 1–100 TeV energies by different γ-ray facilities, is one of the most promising PeVatron candidates. This SNR has a cometary shape, which can be divided into a head and a tail region with different physical conditions. However, in which region the 100 TeV emission is produced has not yet been identified because of the limited position accuracy and/or angular resolution of existing observational data. Additionally, it remains unclear as to whether the origin of the γ-ray emission is leptonic or hadronic.

Aims. With the better angular resolution provided by new MAGIC data compared to earlier γ-ray datasets, we aim to reveal the acceleration site of PeV particles and the emission mechanism by resolving the SNR G106.3+2.7 with 0.1° resolution at TeV energies.

⋆ Corresponding authors: T. Oka, T. Saito, M. Strzys; e-mail: contact.magic@mpp.mpg.de

Methods. We observed the SNR G106.3+2.7 using the MAGIC telescopes for 121.7 h in total – after quality cuts – between May 2017 and August 2019. The analysis energy threshold is ∼0.2 TeV, and the angular resolution is 0.07–0.1°. We examined the γ-ray spectra of different parts of the emission, whilst benefitting from the unprecedented statistics and angular resolution at these energies provided by our new data. We also used measurements at other wavelengths such as radio, X-rays, GeV γ-rays, and 10 TeV γ-rays to model the emission mechanism precisely.
Results. We detect extended γ-ray emission spatially coincident with the radio continuum emission at the head and tail of SNR G106.3+2.7. The fact that we detect a significant γ-ray emission with energies above 6.0 TeV from only the tail region suggests that the emissions above 10 TeV detected with air shower experiments (Milagro, HAWC, Tibet ASγ and LHAASO) are emitted only from the SNR tail. Under this assumption, the multi-wavelength spectrum of the head region can be explained with either hadronic or leptonic models, while the leptonic model for the tail region is in contradiction with the emission above 10 TeV and X-rays. In contrast, the hadronic model could reproduce the observed spectrum at the tail by assuming a proton spectrum with a cutoff energy of ∼1 PeV for that region. Such high-energy emission in this middle-aged SNR (4–10 kyr) can be explained by considering a scenario where protons escaping from the SNR in the past interact with surrounding dense gases at present.
Conclusions. The γ-ray emission region detected with the MAGIC telescopes in the SNR G106.3+2.7 is extended and spatially coincident with the radio continuum morphology. The multi-wavelength spectrum of the emission from the tail region suggests proton acceleration up to ∼PeV, while the emission mechanism of the head region could either be hadronic or leptonic.

Keywords: acceleration of particles – cosmic rays – gamma rays: general – gamma rays: ISM – ISM: clouds – ISM: supernova remnants

1. Introduction

It is widely assumed that cosmic rays (CRs) are accelerated to energies up to ∼PeV at a shock wave in supernova remnants (SNRs) in our Galaxy (see, e.g., Blasi 2013, and references therein). The detection of non-thermal synchrotron X-ray emission in a variety of SNRs (e.g., Koyama et al. 1995) suggests an acceleration of electrons up to hundreds of TeV energies, while the GeV γ-ray emission from SNRs IC 443, W44, and W51C observed with AGILE/*Fermi*-LAT provides evidence for proton acceleration in these objects (Ackermann et al. 2013; Jogler & Funk 2016; Giuliani et al. 2011; Cardillo et al. 2016). However, so far there has been no conclusive observations of SNRs accelerating hadronic particles up to ∼PeV energies, the so-called PeVatrons.

The SNR G106.3+2.7 was first discovered by the northern Galactic plane survey at 408 MHz by the Dominion Radio Astrophysical Observatory (DRAO; Joncas & Higgs 1990). This SNR has a comet-shaped radio morphology, with a bright circular 'head' region and a dimmer 'tail' region elongated to the southeast. The double-component structure of SNR G106.3+2.7 was also observed at a frequency of 2.7 GHz (Furst et al. 1990). The tail region has a marginally softer spectrum than the head region, with $\alpha = 0.70 \pm 0.07$ compared to $\alpha = 0.49 \pm 0.05$, respectively (Pineault & Joncas 2000), with α being the index of flux density $S_\nu \propto \nu^{-\alpha}$. Although the origin of the comet-shaped morphology is not well understood, HI observations suggest this is due to the distribution of the surrounding gases (Kothes et al. 2001). The association of HI and molecular materials with SNR G106.3+2.7 suggests that the distance is 800 pc (Kothes et al. 2001), while the estimation from X-ray absorption is 3 kpc (Halpern et al. 2001b). At the north of the head region, there is an off-centred pulsar wind nebula (PWN) dubbed 'Boomerang'. This latter is powered by the pulsar PSR J2229+6114, which has a characteristic age of 10 kyr and a spin-down luminosity of 2.2×10^{37} erg s^{-1} (Halpern et al. 2001a). The spectrum of the PWN shows a spectral break at 4.3 GHz attributed to synchrotron cooling (Kothes et al. 2006).

In the X-ray band, this SNR was recently studied using the archival *Chandra*, *XMM-Newton*, and *Suzaku* data. In addition to the bright emission from the PWN, non-thermal X-ray emission has been found in both the head and the tail regions (Ge et al. 2021; Fujita et al. 2021). Fujita et al. (2021) claim that the emission in both regions is generated by electrons originating in the PWN, while Ge et al. (2021) argue that the tail emission is more likely due to the electrons accelerated in the shock of the SNR.

Fermi-LAT detected pulsed GeV emission from PSR J2229+6114 (Abdo et al. 2009a), which is associated with the previously unidentified EGRET source 3EG J2227+6122 (Hartman et al. 1999). After subtracting the emission from the pulsar, Xin et al. (2019) found a steady GeV emission in the range of 3–500 GeV from the *Fermi*-LAT data at the tail region. The emission region was better described by a disk of 0.25° radius than a point-like source. In addition, Fang et al. (2022) carefully reanalysed the *Fermi*-LAT data after removing the effect of the pulsed emissions from Boomerang and then obtained consistent results with those of Xin et al. (2019). In Acciari et al. (2009), VERITAS reported a detection of extended very-high-energy (VHE) γ-ray emission in the range of 630 GeV–17 TeV from the tail region. This emission region is ∼0.4° away from the position of PSR J2229+6114, and dubbed VER J2227+608. The shape of this latter is characterised by an elongated two-dimensional Gaussian with a major (minor) axis extending 0.27 ± 0.05 (0.18 ± 0.03)°. The VHE spectrum measured with VERITAS is well fitted by a single power law $\mathrm{d}N/\mathrm{d}E = N_0\ (E/3\,\mathrm{TeV})^{-\Gamma}$ with an index of $\Gamma = 2.29 \pm 0.33_{\mathrm{stat}} \pm 0.30_{\mathrm{sys}}$ and a flux of $N_0 = (1.15 \pm 0.27_{\mathrm{stat}} \pm 0.35_{\mathrm{sys}}) \times 10^{-13}$ cm^{-2} s^{-1} TeV^{-1} (Acciari et al. 2009). Moreover, the GeV emission reported by Xin et al. (2019) is in fact consistent within uncertainties with VER J2227+608 in position, size, and spectrum. The extended γ-ray emission spatially coincides with molecular clouds traced by ^{12}CO ($J = 1{-}0$) emission (Heyer et al. 1998; Kothes et al. 2001), favouring a hadronic origin of the γ-ray emission.

The Milagro collaboration reported the detection of extended VHE γ-ray emission above 20 TeV from the vicinity of the SNR, which is labelled C4 (Abdo et al. 2007) or MGRO J2228+61 (Abdo et al. 2009b; Goodman & Sinnis 2009). HAWC, Tibet ASγ, and LHAASO collaborations also reported the detection of VHE γ-ray emission above tens of TeV from the same region (Albert et al. 2020; Amenomori et al. 2021; Cao et al. 2021). HAWC and Tibet ASγ results suggest a power law spectrum without a cutoff and the spectral indices are $2.25 \pm 0.23_{\mathrm{stat}}$ and $3.17 \pm 0.63_{\mathrm{stat}}$, respectively. Due to the limited angular resolution of air-shower-type detectors, it is not clear whether this emission comes from the head or tail region, while it is significantly offset from the position of PSR J2229+6114. This emission above tens of TeV provides a lower limit on the maximum energy of the particles accelerated in this object. If the

emission process is leptonic, an exponential cutoff energy of the electron must be higher than 270 TeV (Albert et al. 2020) or 190 TeV (Amenomori et al. 2021), while if it is hadronic, the maximum proton energy should be higher than 800 TeV (Albert et al. 2020) or 500 TeV (Amenomori et al. 2021). While it is certain that particles are accelerated to hundreds of TeV in this complex region, it is still inconclusive as to whether the emission originates from hadronic, leptonic, or a combined process. It is also unclear whether parent particles are accelerated in the SNR blast wave or the PWN complex. It should also be noted that the SNR with an age of 4–10 kyr is not expected to accelerate particles to such high energies. In this paper, we study this complex region using deep observations with the Major Atmospheric Gamma Imaging Cherenkov (MAGIC) telescopes, which provide a better angular resolution than those used for previous γ-ray observations of G106.3+2.7. In Sect. 2, we describe the observations that we performed with the MAGIC telescopes. In Sect. 3, we show the observed morphology and spectral properties. In Sect. 4, we show the spectral modelling results for the multi-wavelength spectrum. The origin of the γ-ray emission is discussed in Sect. 5. We summarise the results and discuss future perspectives in Sect. 6.

2. Observation and data reduction

The MAGIC telescopes consist of two 17 m diameter imaging Cherenkov telescopes located at an altitude of 2200 m above sea level at the Observatorio del Roque de los Muchachos on the Canary island La Palma, Spain (28.76° N; 17.89° W). The MAGIC stereoscopic system is able to detect (0.76 ± 0.04)% of the Crab Nebula flux above 210 GeV at 5σ significance in 50 h of observations at medium (30°–45°) zenith angles (Aleksić et al. 2016).

VER J2227+608 was observed from May 2017 to August 2019 for 183.7 h, at zenith angles of between 30° and 50°, yielding an analysis energy threshold of ∼0.2 TeV. The MAGIC angular resolution – which is characterised by the point spread function (PSF) – for this analysis was estimated to be 0.084° (68% containment radius) at $E > 0.2$ TeV and 0.072° at $E >$ 1 TeV, which is the best angular resolution in γ-ray observations achieved for this object so far (e.g., 68% containment radius of the observation with the VERITAS telescope performed in 2009 is 0.11°).

To estimate the background simultaneously, all observations were performed in wobble mode (Fomin et al. 1994) at three positions (RA = 336.31°, Dec = 61.40°; RA = 338.25°, Dec = 61.06°; RA = 336.66°, Dec = 60.42°) with an offset of 0.57° from the position (RA = 337.05°, Dec = 60.96°), which is close to the centre of VER J2227+608 (RA = 337.0°, Dec = 60.8°).

The data analysis was performed with the MAGIC standard analysis package (Zanin 2013). The data selection was based mainly on the transmission of the atmosphere monitored with a LIght Detection And Ranging (LIDAR) system (Fruck et al. 2014). In this analysis, we only selected data with an atmospheric transmission above 85% of the optimum. After quality cuts, the total dead-time-corrected observation time is 121.7 h. We used the wobble map method (e.g., Vovk et al. 2018) for estimating backgrounds. To cross-check the results obtained with the MAGIC standard analysis package, we used the SkyPrism package (Vovk et al. 2018), which includes independent methods to compute the instrument response functions and estimate the energy spectra using a spatial, maximum-likelihood fit. Both results are in good agreement.

3. Results

The pre-trial significance maps around VER J2227+608/SNR G106.3+2.7 in different energy bands are shown in Fig. 1. Panel a shows the morphology of γ rays above 0.2 TeV, indicating that the emission from the direction of VER 2227+608 is clearly detected. Integrating the same area as VERITAS and using Eq. (17) of Li & Ma (1983), the statistical significance is 8.9σ. The area of γ-ray emission is extended and spatially coincident with the radio shell of the SNR, that is, the emission region extends from the SNR head region to the tail region. The emission at the tail coincides with strong ^{12}CO ($J = 1-0$) emission, but the overall emission profile does not closely follow the CO distribution. The emission at the head is seen where ^{12}CO ($J = 1-0$) emission is not observed. It should be noted that ^{12}CO ($J = 1-0$) does not trace all existing interstellar gas, as discussed in Sect. 5.

The panels b–d of Fig. 1 show the maps at 0.2–1.1 TeV, 1.1–6.0 TeV, and 6.0–30 TeV, respectively. The morphology of the detected γ-ray emission clearly changes with energy. By fitting with a symmetric Gaussian function, the centre position of the γ-ray emission in the highest energy band of 6.0–30 TeV is estimated to be (RA, Dec) = (336.66 ± 0.05°, +60.87 ± 0.02°) (J2000), which is offset from the location of PSR J2229+6114 by 0.47 ± 0.03° (panel d). On the other hand, the lower energy emission extends close to the pulsar position (panels b and c). The centroid of the low-energy emission for 0.2–1.1 TeV and its distance from the pulsar position are found to be (RA, Dec) = (336.99 ± 0.04°, +61.04 ± 0.02°) (J2000) and 0.24 ± 0.03°. The 1σ extension at 6.0–30 TeV after removing the effect of PSF is 0.14 ± 0.09°, which is consistent with the value (0.24 ± 0.14°) reported by Tibet ASγ Amenomori et al. (2021).

To better understand the emission mechanism, we studied the γ-ray spectra at the head and tail regions. The parameters of the head and the tail regions are summarised in Table 1 and shown in Fig. 1a. The centres of these regions are obtained from a fit to the γ-ray map above 0.2 TeV (Fig. 1a) with a double symmetric Gaussian. The position of the tail emission is in good agreement with the peak position observed with VERITAS/Tibet (Acciari et al. 2009; Amenomori et al. 2021) and included within the upper limit at 90% confidence level of the Gaussian extension of HAWC J2227+610 (Albert et al. 2020). The spatial distribution in Fig. 1a appears to have a more complex shape than the double symmetric Gaussian function, but as discussed in Appendix A, current statistics allow the data to be fit with this function. The radii of these areas are chosen to be the same for both regions and to be maximised without overlapping. In Fig. 2, we show the so-called θ^2 distributions of the two regions, where θ is the opening angle between the centre of the region and the event arrival direction. For each of the three wobble-pointing positions, two OFF regions were defined such that the ON and the two OFF regions form an equilateral triangle with its centre at the camera centre. The OFF events are estimated by taking the average of these six regions. The excesses are detected from the head and tail regions above 0.2 TeV with statistical significance of 6.2σ and 6.9σ, respectively, evaluated using Eq. (17) of Li & Ma (1983). The significances for 0.2–1.1 TeV are 4.8σ at the head and 2.8σ at the tail, while for 6.0–30 TeV they are 6.5σ at the tail, and only 2.4σ at the head, indicating that the magnitude ratio of the head and the tail emissions is inverted between the low- and high-energy bands.

Figures 3 and 4 show the γ-ray spectra of the two regions defined in Table 1 and the extraction region of VER J2227+608 (Acciari et al. 2009), respectively. Using the

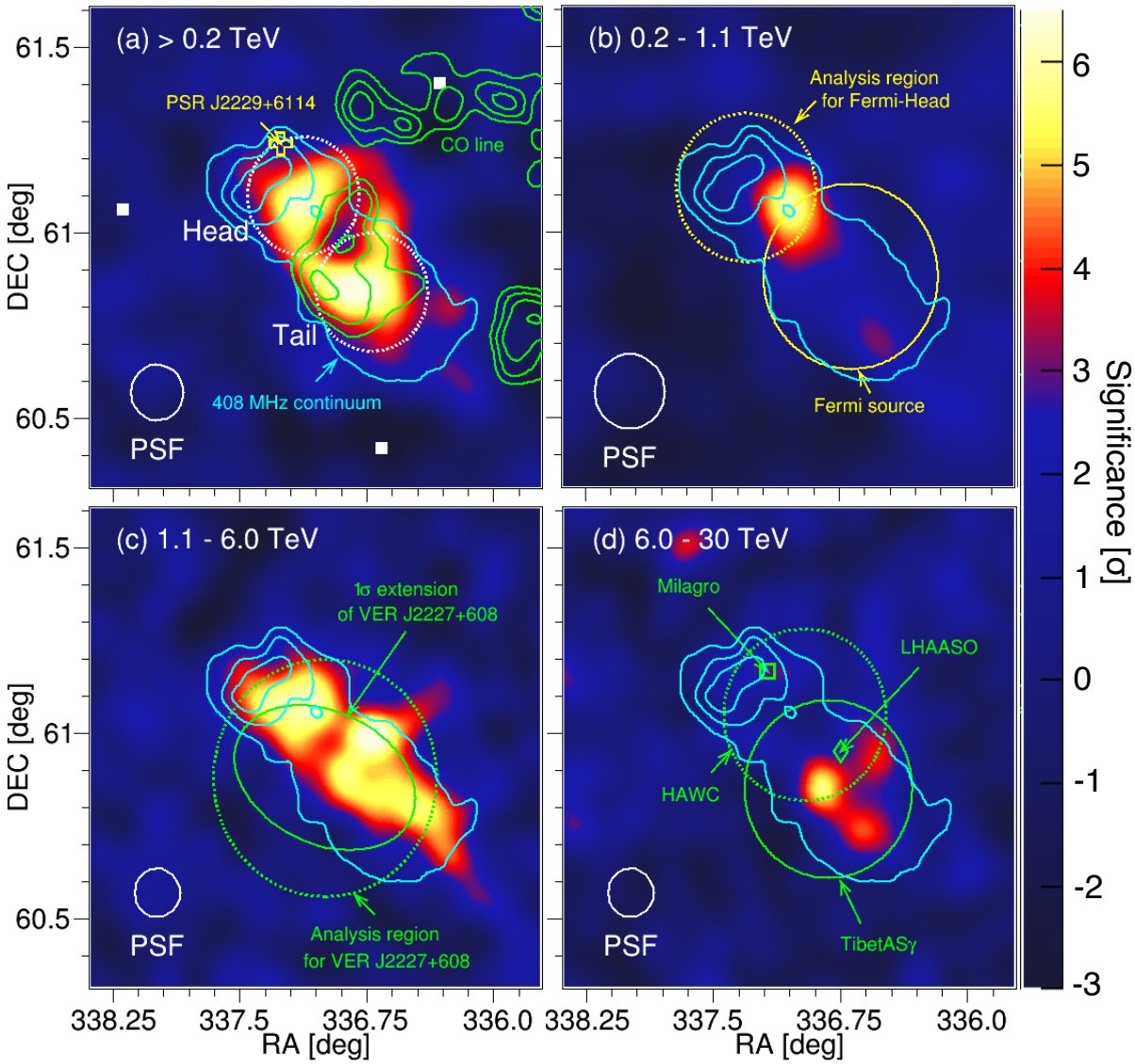

Fig. 1. Energy-dependent pre-trial significance maps of SNR G106.3+2.7 observed with the MAGIC telescopes. (*a*) Map above 0.2 TeV. The white circle labeled 'PSF' represents the 0.075° size of a Gaussian kernel (corresponding to the MAGIC γ-ray PSF) for this analysis. The position of PSR J2229.0+6114 is marked with the open yellow cross. The cyan contours (overlaid on all panels) show the radio emission of SNR G106.3+2.7 at 408 MHz by DRAO (Pineault & Joncas 2000). The green contours represent the ^{12}CO ($J = 1 - 0$) line intensity integrated over the velocity range from −6.41 to −3.94 km s^{-1}. The white dotted circles show θ^2 cut regions of the head and tail regions, respectively, as shown in Table 1. Also shown by white squares are the pointing positions used in the observations. (*b*) Map at 0.2–1.1 TeV. The white circle labelled 'PSF' represents the 0.100° size of a Gaussian kernel, as in panel a. The yellow solid and dotted circles represent the extension and location of the *Fermi*-LAT source (Xin et al. 2019) and the analysis region for the head region used in Liu et al. (2020), respectively. (*c*) Map at 1.1–6.0 TeV. The white circle labelled 'PSF' represents the 0.065° size of a Gaussian kernel, as in panel b. The green ellipse and dotted circles represent the extended TeV γ-ray emission of VER J2227+608 and θ^2 cut region used in the VERITAS paper (Acciari et al. 2009), respectively. (*d*) Map at 6.0–30 TeV. The white circle labelled 'PSF' represents the 0.065° size of a Gaussian kernel, as in panel c. The green solid and dotted circles represent the extended γ-ray emission above 10 TeV observed with Tibet ASγ (Amenomori et al. 2021) and the upper limit at 90% confidence level of the Gaussian extension of HAWC J2227+610 (Albert et al. 2020), respectively. The open square and diamond show the centroid of the VHE γ-ray emission detected with Milagro (Abdo et al. 2009b) and LHAASO (Cao et al. 2021), respectively.

forward-folding method (Aleksić et al. 2016), the spectra are fitted with a power-law function:

$$\frac{\mathrm{d}N}{\mathrm{d}E} = N_0 \left(\frac{E}{3\ \mathrm{TeV}}\right)^{-\Gamma}. \quad (1)$$

The best-fit parameters are summarised in Table 2. The γ-ray spectrum in the tail region has a higher flux and a marginally harder index than that of the head region. For the VER J2227+608, using the same integration region as VERITAS, our results are consistent with those of Acciari et al. (2009) within the statistical uncertainties in both the index and the normalisation at 3 TeV. The apparent discrepancy seen in Fig. 4 between the MAGIC results and the Tibet ASγ measurement at the 6–20 TeV range amounts to a statistical significance of only 1.4σ. Considering the source extension of VER J2227+608 and the MAGIC PSF, the flux derived in this work may correspond to ∼60% of the whole region

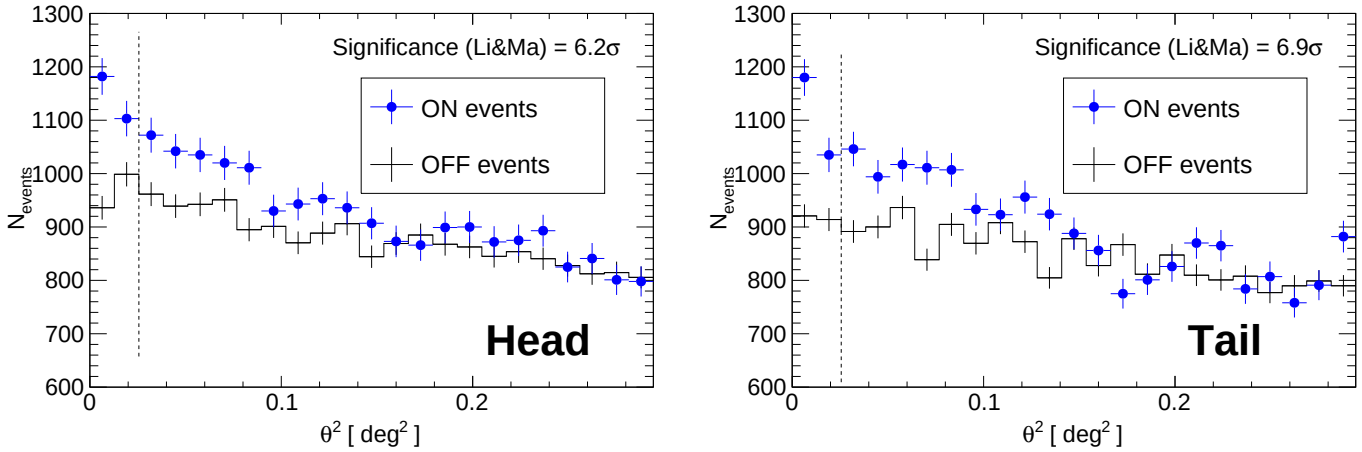

Fig. 2. θ^2 distributions of ON (blue circles) and OFF (black line) events above 0.2 TeV towards the centre of the head region (*left*) and that of the tail region (*right*). The region between zero and the vertical dashed line (at $\theta^2 = 0.0256$ deg^2) was used to estimate ON and OFF events. The OFF data represent the average of six regions rotated by 120 and 240 deg with respect to each wobble centre from the ON region.

Table 1. Regions considered in this work for the analysis of MAGIC data and their modelling.

Source	RA	Dec	Radius
Head region	337.°13	61.°10	0.°16
Tail region	336.°72	60.°84	0.°16

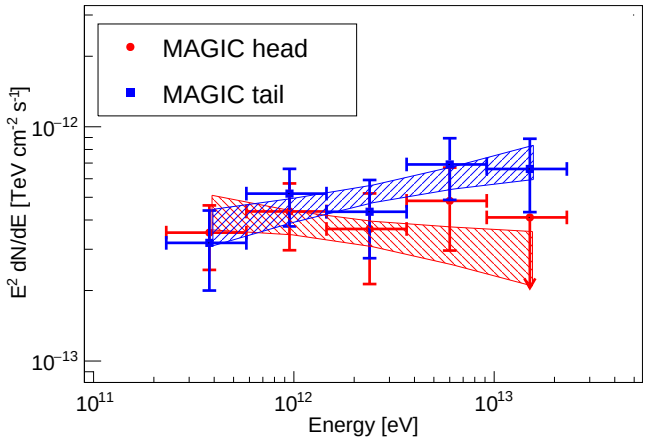

Fig. 3. Energy spectra of the head and tail regions. Red and blue data represent the spectra of the head and tail, respectively. The color 'bow-tie' areas show the result of fitting with a simple power-law function and 1σ statistical uncertainties.

estimated with the other experiments. If this loss is considered, the discrepancy between MAGIC and Tibet ASγ relaxes from 1.4σ to 1.1σ. In addition, if the systematic uncertainties are taken into account, both results agree within 1σ.

4. Modelling

Previous studies (e.g., Liu et al. 2020; Ge et al. 2021; Bao & Chen 2021; Fang et al. 2022) discussed the origin of γ rays using the spectrum up to 100 TeV of the whole region of this object, while the γ-ray spectra of the head and the tail regions are obtained in this work for the first time. Here, we try to model the γ-ray emission mechanism of the head and the tail region individually. Both hadronic and leptonic models are examined using the naima framework introduced by Zabalza (2015).

4.1. Description of VHE γ-ray emission

The spatial coincidence of the MAGIC VHE γ-ray emission and the 408 MHz radio continuum shown in Fig. 1a suggests that the VHE γ-ray emission is associated with the radio SNR G106.3+2.7. On the other hand, as shown in Fig. 1d, the significant γ-ray emission above 6.0 TeV is detected in the tail region but not in the head region. The extracted spectra shown in Fig. 4 suggest that the head contribution to the total flux above 10 TeV is less than 37.1% (2σ upper limit). In the following modelling and discussion, we assume that the measured emission above 10 TeV (Abdo et al. 2009b; Albert et al. 2020; Amenomori et al. 2021; Cao et al. 2021) is only from the tail region.

4.2. SNR G106.3+2.7 and measurements in other wavelengths

The distance to the SNR G106.3+2.7 from the Earth is assumed to be 0.8 kpc (Kothes et al. 2001)[1]. Pineault & Joncas (2000) derived the radio fluxes from the SNR-head and tail, separately. We adopted them since the definition of head and tail are (not perfectly but) nearly identical between this work and Pineault & Joncas (2000). The X-ray spectra for the head and tail regions are taken from results of the "East" and "West" regions from Fujita et al. (2021), respectively, multiplying the intensity by the area of a circle with a radius of 0.16° used in the MAGIC analysis. At GeV range, Xin et al. (2019) and Liu et al. (2020) reported the spectral points and upper limits assuming that the sources have a disk shape. They obtained the radii of 0.20° and 0.25° for the disks. We scaled down their measurements by $(0.16/0.20)^2$ for the head and $(0.16/0.25)^2$ for the *tail*. In this study, we do not consider the direct contributions from the compact Boomerang nebula, whose angular diameter is ~0.05°, because the γ-ray flux of the region is estimated to be ~10% or less of the head region from the radio and X-ray flux (Liu et al. 2020).

[1] Once we assume that the distance is 3 kpc estimated from the X-ray observation (Halpern et al. 2001b) instead of 0.8 kpc, the estimate of SNR size is (3/0.8 kpc) ~ 4 times larger and also the total energy of particles (W) in the modelling is $(3/0.8 \text{ kpc})^2$ ~ 14 times higher. However, these do not affect the results discussed in the text.

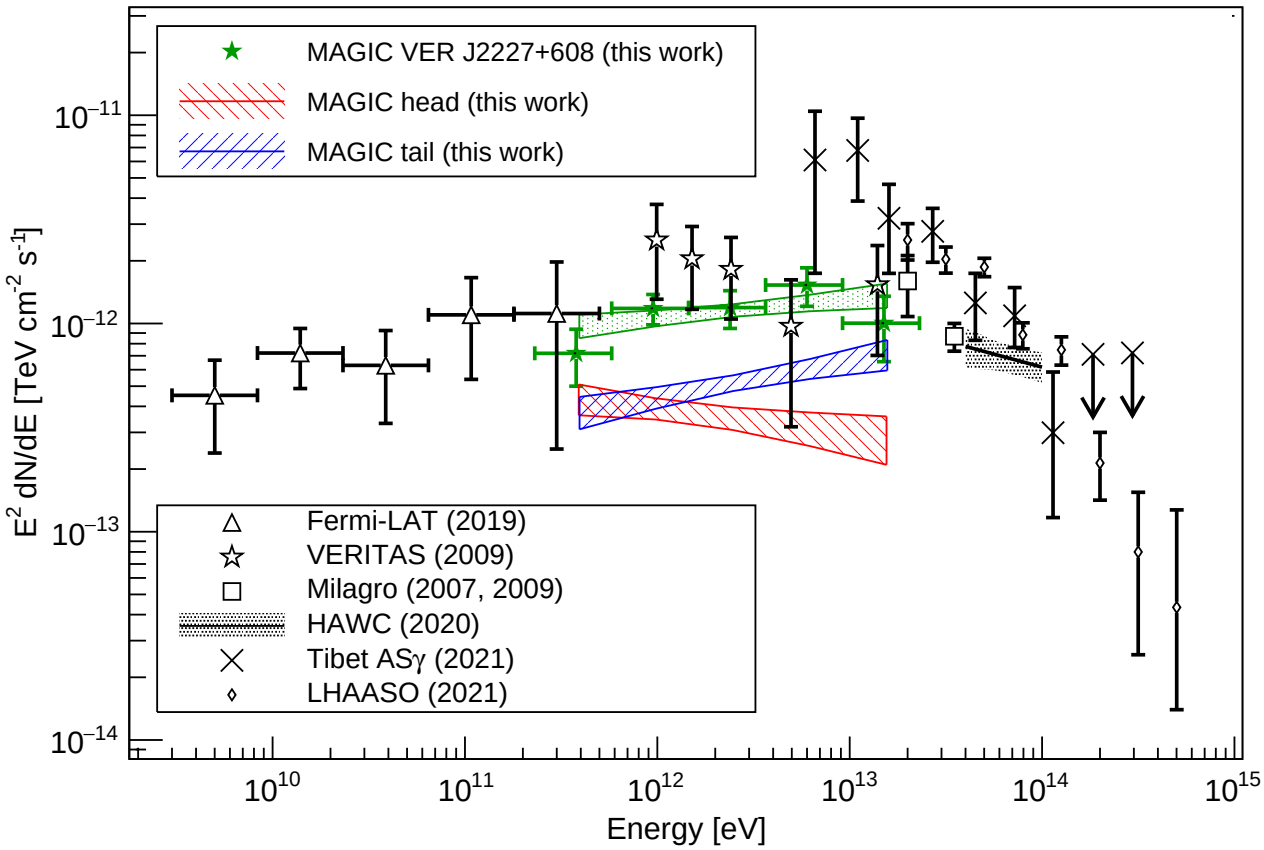

Fig. 4. Spectral energy distribution of the whole region of SNR G106.3+2.7. Green data represent the spectrum of the VER J2227+608 region as measured with the MAGIC telescopes. The shaded blue and red regions show the same areas as in Fig. 3. The open triangles, open stars, open squares, x marks, and open diamonds show the *Fermi*-LAT (Xin et al. 2019), VERITAS (Acciari et al. 2009), Milagro Abdo et al. (2007, 2009b), Tibet ASγ (Amenomori et al. 2021), and LHAASO measurements (Cao et al. 2021), respectively. The black bow-tie area shows a power-law fit and 1σ statistical errors measured by HAWC (Albert et al. 2020).

Table 2. Comparison of the spectral parameters between the MAGIC results reported here and the VERITAS ones (Acciari et al. 2009).

Source	N_0 (10^{-14} cm^{-2} s^{-1} TeV^{-1}) at 3 TeV	Γ	χ^2/ndf
Head	$3.8 \pm 0.7_{\rm stat} \pm 0.7_{\rm sys}$	$2.12 \pm 0.12_{\rm stat} \pm 0.15_{\rm sys}$	5.5/6
Tail	$6.0 \pm 0.7_{\rm stat} \pm 1.0_{\rm sys}$	$1.83 \pm 0.10_{\rm stat} \pm 0.15_{\rm sys}$	2.6/6
VER J2227+608 (MAGIC)	$13.1 \pm 1.1_{\rm stat} \pm 2.1_{\rm sys}$	$1.91 \pm 0.07_{\rm stat} \pm 0.15_{\rm sys}$	7.1/6
VER J2227+608 (VERITAS, Acciari et al. 2009)	$11.5 \pm 2.7_{\rm stat} \pm 3.5_{\rm sys}$	$2.3 \pm 0.33_{\rm stat} \pm 0.30_{\rm sys}$	–

Notes. All sources were fitted with the power-law function of Eq. (1), using a forward-folding method (Aleksić et al. 2016).

4.3. Leptonic model

For the leptonic model, the VHE γ-ray emission can be mainly produced by inverse Compton (IC) scattering (Blumenthal & Gould 1970). The energy spectra of electrons are assumed to follow a power-law function with an exponential cutoff. The cosmic microwave background, a galactic near-infrared (NIR) radiation field, and a galactic far-infrared (FIR) radiation field are considered as seed photon fields in the IC process. Using the model included in the GALPROP package (Porter et al. 2008), the energy density of NIR and FIR are estimated to be 0.1 eV cm^{-3} at T = 30 K and 0.3 eV cm^{-3} at T = 3000 K, respectively. The radio and the non-thermal X-ray emission are produced by high-energy electrons via the synchrotron process.

The following procedure obtained the model parameters: the total amount of electrons is determined to reproduce the γ-ray data with the given target photon density described above, and the magnetic field strength and electron cutoff energy are determined such that the synchrotron reproduces the radio and X-ray data, respectively.

4.4. Hadronic model

For the hadronic model, the γ-ray emission results from the decay of neutral pions produced by inelastic proton-proton (pp) collisions. The energy spectra of protons are assumed to follow a power-law function with an exponential cutoff. The target gas density of each region is estimated using the radio line data of HI and ^{12}CO (J = 1–0), (see Appendix B). As a result, we adopted $n_{\rm HI} + n_{\rm CO} \sim 100\,{\rm cm}^{-3}$ for the head region and $n_{\rm HI} + n_{\rm CO} \sim 200\,{\rm cm}^{-3}$ for the tail region. Furthermore, IC and synchrotron emissions by relativistic electrons are also considered as in Sect. 4.3.

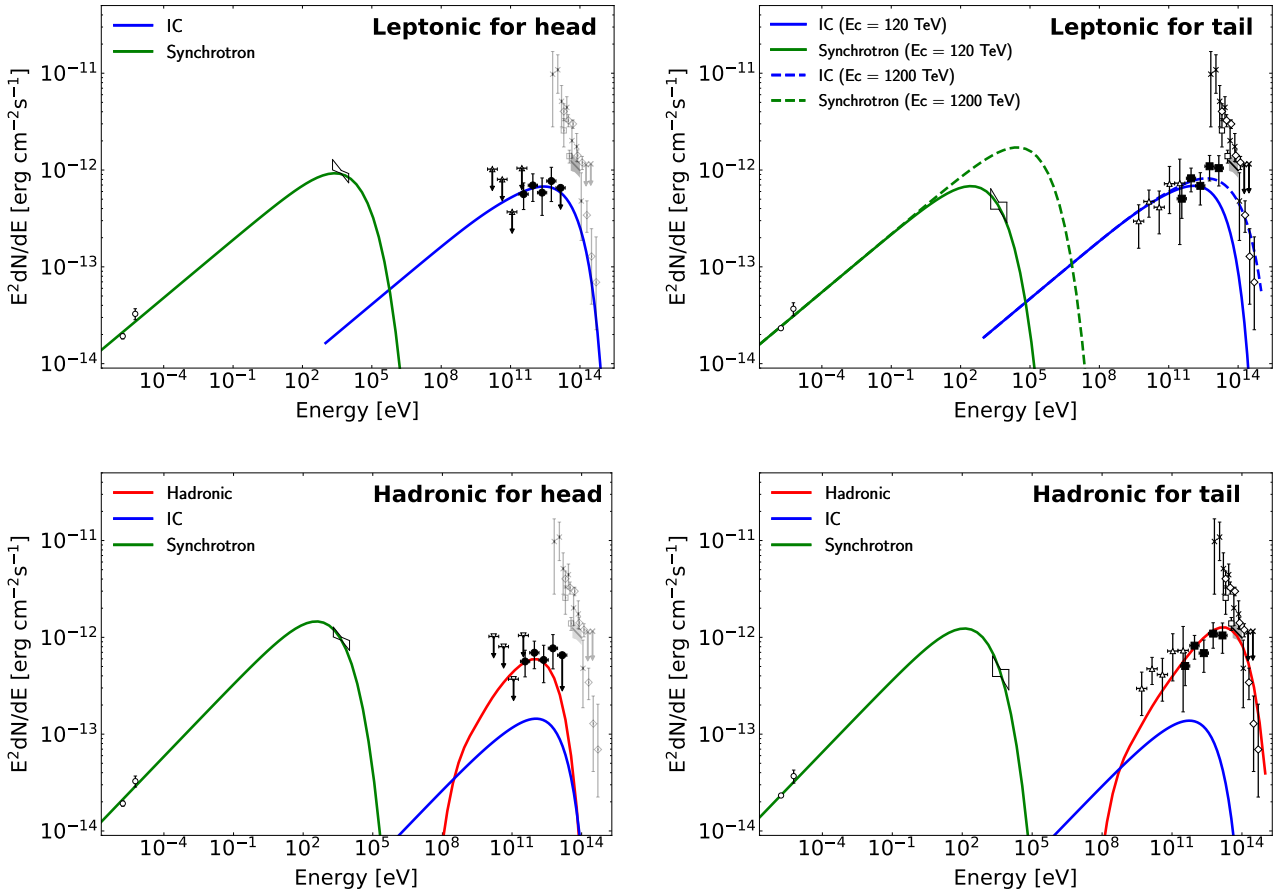

Fig. 5. Modeling of the SED of SNR G106.3+2.7. The *left and right panels* show the results of the head and the tail, respectively. The *top and bottom panels* show the results of the leptonic and hadronic models, respectively. The white circles show the radio flux of each region (Pineault & Joncas 2000). The black bow-tie area shows a power-law fit and 1σ statistical errors measured by Suzaku (Fujita et al. 2021). The open triangles show the *Fermi*-LAT measurements (Xin et al. 2019; Liu et al. 2020). The markers in the TeV γ-ray band are the same as in Fig. 4, but those corresponding to the MAGIC data are shown in black here. The red, blue and green lines show the hadronic, IC and synchrotron emission. The model parameters of each panel are summarized in Table 3. In the *top-right panel*, the solid and dashed lines show the leptonic emission with the energy cutoff of 120 and 1200 TeV, respectively.

The proton spectrum (flux and energy cutoff) is determined to reproduce the γ-ray data, while the electron spectrum is given such that the synchrotron radiation reproduces the radio and X-ray data assuming a magnetic-field strength of 10 μG.

4.5. Results of modelling

Figure 5 shows the modelling result of the leptonic (upper panels) and hadronic (lower panels) models. Parameters for the modelling are summarised in Table 3.

The broad-band spectrum of the head region can be explained well with the leptonic model (χ^2/ndf = 5.0/7[2]). In the case of the tail region, the leptonic model can reproduce the observed data only in the radio, X-ray, *Fermi*-LAT, and MAGIC band (χ^2/ndf = 8.2/13), but fails when including air-shower experiments (χ^2/ndf = 103.1/31). To explain the γ-ray emission above 10 TeV measured by air shower experiments, a high cutoff energy of electrons of ∼1200 TeV is required. However, the synchrotron spectrum produced with such high cutoff energy is excluded by the observed X-ray flux. The χ^2/ndf for the model with the high cutoff energy is found to be $\gg$1 when considering the X-ray data.

For the hadronic model, the γ-ray spectra of both the head and the tail region can be reproduced assuming a proton maximum energy of 60 TeV and 1 PeV, respectively (χ^2/ndf = 5.3/7 and 39.9/31). While the γ-ray emission has a hadronic origin, the observed data in the radio and X-ray band may instead result from synchrotron emission. The parent electron distribution should follow a power-law spectrum different from that of the protons (parameters shown in Table 3).

5. Discussion

5.1. head region

The X-ray emission in the head region exhibits a softening of the spectral index with distance from the pulsar, suggesting that the emission originates in electrons accelerated in and propagated

[2] As the results of the X-ray band (Fujita et al. 2021) and HAWC (Albert et al. 2020) have been given as a fitted power-law function, the flux and statistical uncertainty only at the normalisation energy of the fit are considered in the calculation of the chi-squared statistic. In addition, these calculations for γ-ray observation data take into account not only statistical errors but also systematic errors on the normalisation flux. As the systematic errors for the *Fermi*-LAT and LHAASO results were not estimated in the previous papers for this source, we estimate those of *Fermi*-LAT and LHAASO with the uncertainties of the effective area (`https://fermi.gsfc.nasa.gov/ssc/data/analysis/scitools/Aeff_Systematics.html`) and absolute energy scale (Aharonian et al. 2021), respectively.

Table 3. Model parameters for reproducing the observed spectra.

Model	Source	α_e	$E_{c,e}$ [TeV]	W_e [erg]	B [μG]	α_p	$E_{c,p}$ [TeV]	W_p [erg]	N_{gas}[cm^{-3}]	χ^2/ndf
Leptonic	Head	2.6	360	1.4×10^{47}	3	–	–	–	–	5.0/7
	Tail	2.6	120 (1200)$^{(\dagger)}$	1.6×10^{47}	3	–	–	–	–	103.1/31 ($\gg$ 1)$^{(\dagger)}$
Hadronic	Head	2.5	60	1.8×10^{46}	10	1.7	60	8.9×10^{45}	100	5.3/7
	Tail	2.5	35	2.0×10^{46}	10	1.7	1000	8.2×10^{45}	200	39.9/31

Notes. α and E_c are the power-law index and the cutoff energy of the particle spectrum, respectively. W is the total energy of particles with energy above 1 GeV. The subscript e and p denote electrons and protons. B is the magnetic-field strength in unit of μG. N_{gas} is the target gas density in unit of cm^{-3}. $^{(\dagger)}$In the top-right panel of Fig. 5, the model curve using the value in the parentheses is shown with the dashed line.

from the shock of the PWN (Ge et al. 2021). Our modelling result shows that X-ray and γ-ray fluxes can be explained with leptonic emission from the same electron population. This implies that the γ-ray emission can originate in the PWN. Assuming the electron cutoff energy ($E_{c,e}$) and the magnetic-field strength (B) used in the leptonic model for the head region, the electron lifetime due to synchrotron losses is given by: ∼3.9 kyr $(E_{c,e}/360\ \mathrm{TeV})^{-1}(B/3\ \mu\mathrm{G})^{-2}$, which is consistent with the age of the SNR estimated to be 3.9 kyr from the spectral break in the radio spectrum of the PWN (Kothes et al. 2006) or 10 kyr from the pulsar spin-down age (Halpern et al. 2001a).

A hadronic scenario also works for the head. The protons accelerated up to 60 TeV can explain the VHE γ-ray emission detected by MAGIC, given the presence of dense HI clouds in the head region pointed out by Kothes et al. (2001). Although CO emission is not prominent, HI/CO intensity suggests the presence of gases with a total proton density of ∼100 cm^{-3}, which is sufficient for the pp emission, as derived in Appendix B. Still, electrons with a largely different spectral index are needed to explain the radio and X-ray emission. One of the simplest explanations would be that electrons are mainly from the PWN, while the protons are accelerated in the shell. Acceleration up to 60 TeV by a 3 kyr SNR is possible (Cardillo et al. 2015), while an electron lifetime due to the synchrotron cooling is ∼2.2 kyr $(E_{c,e}/60\ \mathrm{TeV})^{-1}(B/10\ \mu\mathrm{G})^{-2}$.

5.2. Tail region

The modelling described in the previous section suggests that it is difficult to explain the tail emission with the leptonic model. On the other hand, the hadronic model worked well; the γ-ray spectrum of the tail region can be reproduced assuming a proton maximum energy of 1 PeV (χ^2/ndf = 39.9/31). Generally speaking, acceleration up to 1 PeV can only be achieved at the early stages (< 1.0 kyr) of SNR evolution (e.g., Bell et al. 2013; Cardillo et al. 2015; Cristofari et al. 2021, 2022). However, as mentioned in Sect. 5.1, the age of this SNR has been estimated to be 3.9 kyr from the spectral break in the radio spectrum of the PWN (Kothes et al. 2006) or 10 kyr from the pulsar spin-down age (Halpern et al. 2001a). This discrepancy in the SNR age can be solved assuming a CR-escape scenario (e.g., Aharonian & Atoyan 1996; Gabici & Aharonian 2007), whereby protons accelerated up to ∼ PeV energies at a young SNR escape from acceleration regions and illuminate nearby clouds, which produce 'delayed' γ-ray emission. This scenario can also explain a proton index of 1.7, which is harder than the index of 2.0 expected from diffusive shock acceleration (DSA), (e.g., Bell 1978; Blandford & Ostriker 1978). On the other hand, it requires high-density clouds that spatially coincide with the γ-ray morphology. Using the CGPS data of HI and ^{12}CO (J = 1–0), (see Appendix B), we confirm the coincidence of the γ-ray emission with CO line emission in the velocity range −6.41 to −3.94 km s^{-1} in the tail region, which was already pointed out by Kothes et al. (2001) and Acciari et al. (2009). This supports the CR-escape scenario in the tail region. This scenario is consistent with the interpretation given by Albert et al. (2020), Fujita et al. (2021), and Amenomori et al. (2021). The authors estimated the diffusion length of CRs using the relation $l_{\mathrm{diff}} = \sqrt{Dt}$, where D is the diffusion coefficient and t is the diffusion time. The authors then found, even assuming a small diffusion coefficient ($D \sim 10^{26}$ cm^2 s^{-1} at GeV), that the diffusion length for CRs with an energy of O(100 TeV) in 5–10 kyr is larger (40–60 pc) than the size of the SNR (∼6 pc) and thus suggested the CRs are not confined in the SNR. A cloud with a radius of a few parsec located at 40–60 pc away is a plausible target considering the energetics of the supernova.

Electrons may also escape in the same way as protons but be affected by radiative cooling, which is not considered in the modelling. However, the change in the spectral index due to the cooling effect is estimated to be at most 0.1–0.4 (Diesing & Caprioli 2019), suggesting that the difference (∼0.8) between the proton and electron indices cannot be explained even by considering it. This fact implies that leptonic and hadronic emissions may be produced at different locations and thus under different physical conditions. For example, leptonic emission comes from the SNR shell, while hadronic emission comes from the interstellar gas spatially separated from the SNR. This assumption can allow the unusual ratio of the total energy of CRs ($W_p \lesssim W_e$) because only the hadronic emission is affected by the propagation effect (Gabici & Aharonian 2007), and thus only W_p decreases. We note that the electron lifetime due to synchrotron losses is estimated to be ∼3.6 kyr $(E_{c,e}/35\ \mathrm{TeV})^{-1}(B/10\ \mu\mathrm{G})^{-2}$, which is in good agreement with the SNR age.

The hard proton index found in the TeV band can also be explained with SNR–cloud interactions (Inoue et al. 2012), as an alternative to the CR-escape scenario. However, the maximum energy of ≳PeV in SNRs older than 1 kyr cannot be explained with this model. Also, the scenario could not explain the differences in the distribution of electrons and protons (Diesing & Caprioli 2019), as mentioned above.

5.3. Remarks on the discussion

The integrated region of MAGIC-tail in this analysis may miss a fraction of the γ-ray emissions observed by air-shower experiments. Using the Gaussian extension at >6 TeV derived with the θ^2 plot around the tail, the event fraction surviving the θ^2

cut is estimated to be 74%–95% (1σ uncertainty). We examined the effect of the flux of air-shower experiments scaled down by 26% on our model fit for the tail spectrum. In the leptonic model, χ^2/ndf changed only slightly (from 103.1/31 to 96.3/31), indicating that the model is still inconsistent with the observed data. In the hadronic model, χ^2/ndf also changed (from 39.9/31 to 41.3/31), and the model still works. As a result, the underestimation of the flux due to the angular cuts does not affect our conclusion.

It should also be noted that the data points of Milagro, HAWC, TibetASγ, and LHAASO, included in the modelling of the tail spectrum, are from extraction regions which partially include the head. They are therefore potentially contaminated if the head emits radiation >10 TeV. Even if, for example, half of the emission above 10 TeV were found to come from the head, this would not explain the tail emission with this rather simple leptonic model.

Though more complicated leptonic models – such as that with two electron populations with adjusted magnetic field strengths – can explain the tail emission as demonstrated in Ge et al. (2021), exploring all possible scenarios with the currently available data is beyond the scope of this paper. To accurately determine the emission mechanism, it is first necessary to also separate the extraction regions at the head and tail for spectral points above 10 TeV.

6. Summary

We carried out deep γ-ray observations of SNR G106.3+2.7 with the MAGIC telescopes. The MAGIC observations revealed a γ-ray morphology that is spatially coincident with the radio emission and achieved a significant detection of TeV γ rays from the head and the tail regions of SNR G106.3+2.7 for the first time. The energy spectra in energy regimes from 0.2 TeV to 20 TeV of the head and tail regions can be well described by a simple power-law function of $\mathrm{d}N/\mathrm{d}E = N_0\ (E/3\,\mathrm{TeV})^{-\Gamma}$ with the indices of $\Gamma = 2.12 \pm 0.12$ and 1.83 ± 0.10, respectively. The total flux of the two regions is consistent with the VERITAS results within the statistical uncertainty. As the emission above 10 TeV is seen only from the tail region, it is likely that the γ rays above 10 TeV detected with the air shower experiments (e.g., Abdo et al. 2009b) are mainly emitted from the SNR tail. We investigated the possibility of explaining the emission from the two regions. The head emission can be explained with both a hadronic and a leptonic model. Under the assumption that the γ-ray emission above 10 TeV is only from the tail region, the leptonic model emission of the tail region is in contradiction with the X-ray flux. The proton spectrum with the cutoff at ~1 PeV could explain the observed spectrum from the tail region. It may suggest that protons accelerated in the SNR shock in the past escaped from the SNR and interacted with target gas located in front of the SNR along the line of sight. This scenario could also explain the inconsistency between the SNR age and maximum energy of accelerated protons. By considering complex particle distributions and/or magnetic field environments, the leptonic model may explain the observed spectra (e.g., Ge et al. 2021), but this is beyond the scope of this paper. For a better determination of the VHE γ-ray origin, it is necessary to observe the γ-ray emission >10 TeV with a high sensitivity and with an angular resolution of greater than 0.1°, which would be sufficient to resolve the two regions and quantitatively evaluate the difference between the cutoff energies in the head and tail. For example, with the current MAGIC telescopes, more than ~3600 h would be required to detect 20–200 TeV emission at the tail. Such observations could be possible with the new generation of γ-ray observatories, CTA/ASTRI (Bernlöhr et al. 2013; Lombardi et al. 2021).

Acknowledgements. We thank Hidetoshi Sano, Tsuyoshi Inoue and Yasuo Fukui for the fruitful discussion. We would like to thank the Instituto de Astrofísica de Canarias for the excellent working conditions at the Observatorio del Roque de los Muchachos in La Palma. The financial support of the German BMBF, MPG and HGF; the Italian INFN and INAF; the Swiss National Fund SNF; the grants PID2019-104114RB-C31, PID2019-104114RB-C32, PID2019-104114RB-C33, PID2019-105510GB-C31, PID2019-107847RB-C41, PID2019-107847RB-C42, PID2019-107847RB-C44, PID2019-107988GB-C22 funded by MCIN/AEI/ 10.13039/501100011033; the Indian Department of Atomic Energy; the Japanese ICRR, the University of Tokyo, JSPS, and MEXT; the Bulgarian Ministry of Education and Science, National RI Roadmap Project DO1-400/18.12.2020 and the Academy of Finland grant nr. 320045 is gratefully acknowledged. This work was also been supported by Centros de Excelencia "Severo Ochoa" y Unidades "María de Maeztu" program of the MCIN/AEI/ 10.13039/501100011033 (SEV-2016-0588, SEV-2017-0709, CEX2019-000920-S, CEX2019-000918-M, MDM-2015-0509-18-2) and by the CERCA institution of the Generalitat de Catalunya; by the Croatian Science Foundation (HrZZ) Project IP-2016-06-9782 and the University of Rijeka Project uniri-prirod-18-48; by the DFG Collaborative Research Centres SFB1491 and SFB876/C3; the Polish Ministry Of Education and Science grant No. 2021/WK/08; and by the Brazilian MCTIC, CNPq and FAPERJ. T. Oka: MAGIC data analysis, paper drafting and edition; T. Saito: project leadership, MAGIC analysis cross-check, paper drafting and edition; M. Strzys: MAGIC analysis cross-check, paper drafting and edition. The rest of the authors have contributed in one or several of the following ways: design, construction, maintenance and operation of the instrument(s) used to acquire the data; preparation and/or evaluation of the observation proposals; data acquisition, processing, calibration and/or reduction; production of analysis tools and/or related Monte-Carlo simulations; discussion and approval of the contents of the draft.

References

Abdo, A., Allen, B., Berley, D., et al. 2007, ApJ, 664, L91
Abdo, A., Ackermann, M., Ajello, M. A., et al. 2009a, ApJ, 706, 1331
Abdo, A., Allen, B. T., Aune, T., et al. 2009b, ApJ, 700, L127
Acciari, V. A., Aliu, E., Arlen, T., et al. 2009, ApJ, 703, L6
Ackermann, M., Ajello, M., Allafort, A., et al. 2013, Science, 339, 807
Aharonian, F. A., & Atoyan, A. M. 1996, A&A, 309, 917
Aharonian, F., An, Q. A., Bai, L. X., et al. 2021, Phys. Rev. D, 104, 062007
Albert, A., Alfaro, R., Alvarez, C., et al. 2020, ApJ, 896, L29
Aleksić, J., Ansoldi, S., Antonelli, L. A., et al. 2016, Astropart. Phys., 72, 76
Amenomori, M., Bao, Y. W., Bi, X. J., et al. 2021, Nat. Astron., 5, 460
Bao, Y., & Chen, Y. 2021, ApJ, 919, 32
Bell, A. R. 1978, MNRAS, 182, 147
Bell, A., Schure, K., Reville, B., & Giacinti, G. 2013, MNRAS, 431, 415
Bernlöhr, K., Barnacka, A., Becherini, Y., et al. 2013, Astropart. Phys., 43, 171
Blandford, R., & Ostriker, J. 1978, ApJ, 221, L29
Blasi, P. 2013, A&ARv, 21, 70
Blumenthal, G. R., & Gould, R. J. 1970, Rev. Mod. Phys., 42, 237
Bolatto, A. D., Wolfire, M., & Leroy, A. K. 2013, Ann. Rev. Astron. Astrophys., 51, 207
Cao, Z., Aharonian, F. A., An, Q., et al. 2021, Nature, 594, 33
Cardillo, M., Amato, E., & Blasi, P. 2015, Astropart. Phys., 69, 1
Cardillo, M., Amato, E., & Blasi, P. 2016, A&A, 595, A58
Cristofari, P., Blasi, P., & Caprioli, D. 2021, A&A, 650, A62
Cristofari, P., Blasi, P., & Caprioli, D. 2022, ApJ, 930, 28
Dickey, J. M., & Lockman, F. J. 1990, ARA&A, 28, 215
Diesing, R., & Caprioli, D. 2019, Phys. Rev. Lett., 123, 071101
Fang, K., Kerr, M., Blandford, R., Fleischhack, H., & Charles, E. 2022, Phys. Rev. Lett., 129, 071101
Fomin, V., Stepanian, A., Lamb, R., et al. 1994, Astropart. Phys., 2, 137
Fruck, C., Gaug, M., Zanin, R., et al. 2014, in Proceedings, 33rd International Cosmic Ray Conference (ICRC2013): Rio de Janeiro, Brazil, July 2–9, 2013, 1054
Fujita, Y., Bamba, A., Nobukawa, K. K., & Matsumoto, H. 2021, ApJ, 912, 133
Furst, E., Reich, W., Reich, P., & Reif, K. 1990, A&AS, 85, 691
Gabici, S., & Aharonian, F. A. 2007, ApJ, 665, L131
Ge, C., Liu, R.-Y., Niu, S., Chen, Y., & Wang, X.-Y. 2021, The Innovation, 2, 100118
Giuliani, A., Cardillo, M., Tavani, M., et al. 2011, ApJ, 742, L30
Goodman, J., & Sinnis, G. 2009, ATel, 2172, 1

Halpern, J., Camilo, F., Gotthelf, E., et al. 2001a, ApJ, 552, L125
Halpern, J., Gotthelf, E., Leighly, K., & Helfand, D. 2001b, ApJ, 547, 323
Hartman, R., Bertsch, D. L., Bloom, S. D., et al. 1999, ApJS, 123, 79
Heyer, M. H., Brunt, C., Snell, R. L., et al. 1998, ApJS, 115, 241
Inoue, T., Yamazaki, R., Inutsuka, S.-i., & Fukui, Y. 2012, ApJ, 744, 71
Jogler, T., & Funk, S. 2016, ApJ, 816, 100
Joncas, G., & Higgs, L. A. 1990, A&AS, 82, 113
Kothes, R., Uyaniker, B., & Pineault, S. 2001, ApJ, 560, 236
Kothes, R., Reich, W., & Uyanıker, B. 2006, ApJ, 638, 225
Koyama, K., Petre, R., Gotthelf, E. V., et al. 1995, Nature, 378, 255
Landecker, T., Dewdney, P. E., Burgess, T. A. et al. 2000, A&AS, 145, 509
Li, T.-P., & Ma, Y.-Q. 1983, ApJ, 272, 317
Liu, S., Zeng, H., Xin, Y., & Zhu, H. 2020, ApJ, 897, L34
Lombardi, S., Antonelli, L. A., Bigongiari, C., et al. 2021, PoS, ICRC2021, 884
Pineault, S., & Joncas, G. 2000, AJ, 120, 3218
Porter, T. A., Moskalenko, I. V., Strong, A. W., Orlando, E., & Bouchet, L. 2008, ApJ, 682, 400
Taylor, A. R., Gibson, S. J., Peracaula, M., et al. 2003, AJ, 125, 3145
Vovk, I., Strzys, M., & Fruck, C. 2018, A&A, 619, A7
Xin, Y., Zeng, H., Liu, S., Fan, Y., & Wei, D. 2019, ApJ, 885, 162
Zabalza, V. 2015, Proc. Int. Cosmic Ray Conf., 34, 922
Zanin, R. 2013, Int. Cosmic Ray Conference, 33, 0773

[1] Japanese MAGIC Group: Institute for Cosmic Ray Research (ICRR), The University of Tokyo, Kashiwa, 277-8582 Chiba, Japan
[2] Instituto de Astrofísica de Canarias and Dpto. de Astrofísica, Universidad de La Laguna, 38200 La Laguna, Tenerife, Spain
[3] Instituto de Astrofísica de Andalucía-CSIC, Glorieta de la Astronomía s/n, 18008 Granada, Spain
[4] National Institute for Astrophysics (INAF), 00136 Rome, Italy
[5] Università di Udine and INFN Trieste, 33100 Udine, Italy
[6] Max-Planck-Institut für Physik, 80805 München, Germany
[7] Università di Padova and INFN, 35131 Padova, Italy
[8] Institut de Física d'Altes Energies (IFAE), The Barcelona Institute of Science and Technology (BIST), 08193 Bellaterra (Barcelona), Spain
[9] Technische Universität Dortmund, 44221 Dortmund, Germany
[10] Croatian MAGIC Group: University of Zagreb, Faculty of Electrical Engineering and Computing (FER), 10000 Zagreb, Croatia
[11] IPARCOS Institute and EMFTEL Department, Universidad Complutense de Madrid, 28040 Madrid, Spain
[12] Centro Brasileiro de Pesquisas Físicas (CBPF), 22290-180 URCA, Rio de Janeiro (RJ), Brazil
[13] University of Lodz, Faculty of Physics and Applied Informatics, Department of Astrophysics, 90-236 Lodz, Poland
[14] Deutsches Elektronen-Synchrotron (DESY), 15738 Zeuthen, Germany
[15] ETH Zürich, 8093 Zürich, Switzerland
[16] Università di Pisa and INFN Pisa, 56126 Pisa, Italy
[17] Universitat de Barcelona, ICCUB, IEEC-UB, 08028 Barcelona, Spain
[18] Armenian MAGIC Group: A. Alikhanyan National Science Laboratory, 0036 Yerevan, Armenia
[19] Centro de Investigaciones Energéticas, Medioambientales y Tecnológicas, 28040 Madrid, Spain
[20] Department for Physics and Technology, University of Bergen, 5007 Bergen, Norway
[21] INFN MAGIC Group: INFN Sezione di Catania and Dipartimento di Fisica e Astronomia, University of Catania, 95123 Catania, Italy
[22] INFN MAGIC Group: INFN Sezione di Torino and Università degli Studi di Torino, 10125 Torino, Italy
[23] INFN MAGIC Group: INFN Sezione di Bari and Dipartimento Interateneo di Fisica dell'Università e del Politecnico di Bari, 70125 Bari, Italy
[24] Croatian MAGIC Group: University of Rijeka, Faculty of Physics, 51000 Rijeka, Croatia
[25] Universität Würzburg, 97074 Würzburg, Germany
[26] University of Geneva, Chemin d'Ecogia 16, 1290 Versoix, Switzerland
[27] Finnish MAGIC Group: Finnish Centre for Astronomy with ESO, University of Turku, 20014 Turku, Finland
[28] Departament de Física, and CERES-IEEC, Universitat Autònoma de Barcelona, 08193 Bellaterra, Spain
[29] Japanese MAGIC Group: Physics Program, Graduate School of Advanced Science and Engineering, Hiroshima University, 739-8526 Hiroshima, Japan
[30] Armenian MAGIC Group: ICRANet-Armenia, 0019 Yerevan, Armenia
[31] Croatian MAGIC Group: University of Split, Faculty of Electrical Engineering, Mechanical Engineering and Naval Architecture (FESB), 21000 Split, Croatia
[32] Croatian MAGIC Group: Josip Juraj Strossmayer University of Osijek, Department of Physics, 31000 Osijek, Croatia
[33] Japanese MAGIC Group: Department of Physics, Tokai University, Hiratsuka, 259-1292 Kanagawa, Japan
[34] Università di Siena and INFN Pisa, 53100 Siena, Italy
[35] Saha Institute of Nuclear Physics, A CI of Homi Bhabha National Institute, Kolkata 700064, West Bengal, India
[36] Inst. for Nucl. Research and Nucl. Energy, Bulgarian Academy of Sciences, 1784 Sofia, Bulgaria
[37] Japanese MAGIC Group: Department of Physics, Yamagata University, Yamagata 990-8560, Japan
[38] Finnish MAGIC Group: Space Physics and Astronomy Research Unit, University of Oulu, 90014 Oulu, Finland
[39] Japanese MAGIC Group: Department of Physics, Kyoto University, 606-8502 Kyoto, Japan
[40] Japanese MAGIC Group: Institute for Space-Earth Environmental Research and Kobayashi-Maskawa Institute for the Origin of Particles and the Universe, Nagoya University, 464-6801 Nagoya, Japan
[41] Croatian MAGIC Group: Ruđer Bošković Institute, 10000 Zagreb, Croatia
[42] INFN MAGIC Group: INFN Sezione di Perugia, 06123 Perugia, Italy
[43] INFN MAGIC Group: INFN Roma Tor Vergata, 00133 Roma, Italy
[44] Japanese MAGIC Group: Department of Physics, Konan University, Kobe, Hyogo 658-8501, Japan
[45] International Center for Relativistic Astrophysics (ICRA), Rome, Italy
[46] Port d'Informació Científica (PIC), 08193 Bellaterra (Barcelona), Spain
[47] Ruhr-Universität Bochum, Fakultät für Physik und Astronomie, Astronomisches Institut (AIRUB), 44801 Bochum, Germany
[48] University of Innsbruck, Institute for Astro- and Particle Physics, University of Innsbruck, A-6020 Innsbruck, Austria
[49] Dipartimento di Fisica, Università di Trieste, 34127 Trieste, Italy
[50] University of Lodz, Faculty of Physics and Applied Informatics, Department of Astrophysics, 90-236 Lodz, Poland

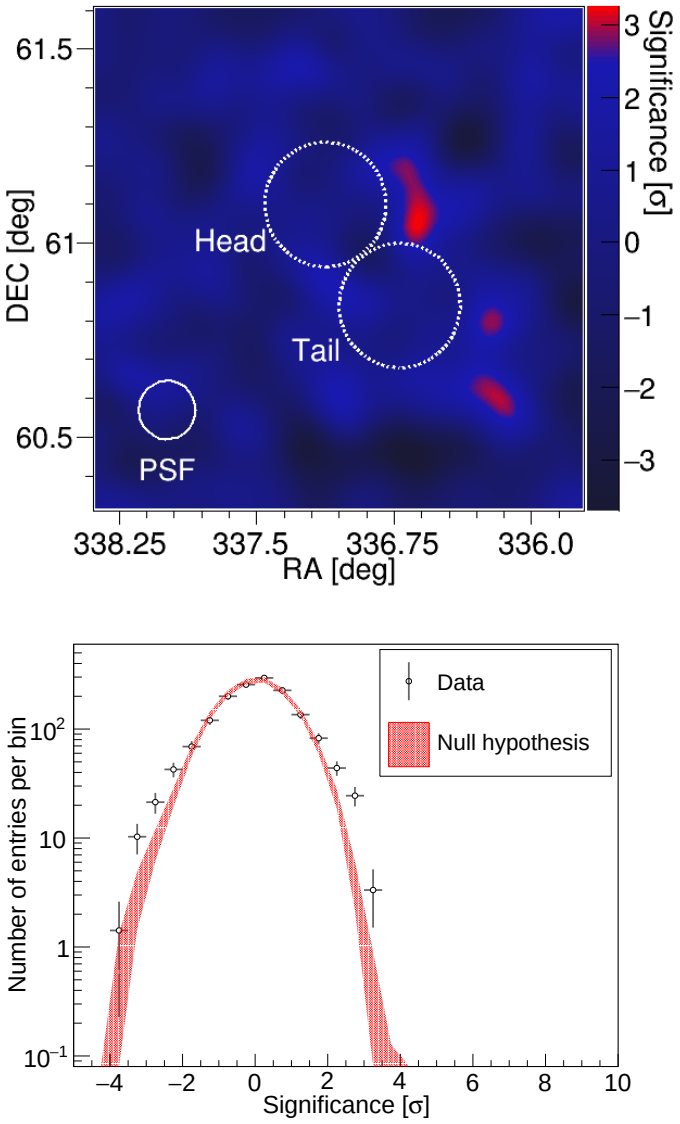

Fig. A.1. Pre-trial significance map (top) and histogram (bottom) of γ rays above 0.2 TeV after subtracting two Gaussian sources. As for the Gaussian parameters, the locations are the same as the definition of head and tail and each 1σ extension radius is 0.085°.

Appendix A: More detailed morphological investigations

We used a double symmetric Gaussian function to examine the radiation peaks and select the analysis regions in the least biased way possible. The best-fit parameters are as in Table 1 for the centre position, and 0.083° (0.087°) for the 1σ extension of the head (tail). Figure A.1 shows the residual map after subtracting two Gaussian sources and its significance distribution of the residuals. The distribution is consistent with the null hypothesis, which indicates that, with the current statistics, the double Gaussian assumption is valid, though the true γ-ray source morphology may be more complex.

Although we cannot claim the proper source shape of the head and tail components from the present statistics, under the assumption that the source has Gaussian-like extension with 1σ of 0.085° (after removing the effect of PSF), the loss and contamination rate from the θ^2 cut are estimated to be 23.5% and 2.7%, respectively. Further observations with better angular resolution could be helpful to determine a proper morphological model.

Table B.1. Gas density of the hydrogen atoms in the head and tail regions. $n_{\rm HI}$ and $n_{\rm CO}$ are estimated with the HI line and ^{12}CO ($J = 1-0$) line data, respectively.

Velocity range [km s^{-1}]	−7.23 – −5.59	−6.41 – −3.94
$n_{\rm HI}$ at head [cm^{-3}]	42	59
$n_{\rm CO}$ at head [cm^{-3}]	73	66
$n_{\rm HI}$ at tail [cm^{-3}]	38	55
$n_{\rm CO}$ at tail [cm^{-3}]	137	191

Appendix B: Gas density in the emission regions

We calculated the gas density in the two regions of SNR G106.3+2.7 with the following outline. We used the data of HI line measured with the Dominion Radio Astronomy Observatory (DRAO) Synthesis Telescope (Landecker et al. 2000) and ^{12}CO ($J = 1-0$) line measured with the Five College Radio Astronomy Observatory (FCRAO; Heyer et al. 1998) from the Canadian Galactic Plane Survey (CGPS; Taylor et al. 2003) database. These observations were carried out with the velocity resolution of 0.824 km s^{-1} at HI line and 0.98 km s^{-1} at CO line. The following relationship was used to calculate the column density: $N_{\rm H}\,[{\rm cm}^{-2}] = X \int_{v_{\rm min}}^{v_{\rm max}} T(v)dv$, where v is the radial velocity, $T(v)$ is the observed brightness temperature (K), and X is the conversion factor (Dickey & Lockman 1990). HI-to-$N_{\rm HI}$ and CO-to-$N_{\rm H_2}$ are given by $X_{\rm HI} = 1.823 \times 10^{18}$ (Dickey & Lockman 1990) and $X_{\rm CO} = 2.0 \times 10^{20}$ (Bolatto et al. 2013). Figure B.1 shows the radial profiles of HI and ^{12}CO ($J = 1-0$) line. There is a significant velocity dependence of the column density, especially in the CO data, which is a concern because the uncertainty of the velocity range affects the calculation of the gas density. Here, we consider two cases of velocity ranges associated with SNR G106.3+2.7: (i) −7.23 to −5.59 km s^{-1} suggested by Kothes et al. (2001) and (ii) −6.41 to −3.94 km s^{-1} suggested by Acciari et al. (2009) and Albert et al. (2020). The clouds associated with the production of the observed γ-ray emission are assumed to be a spherical region around the emission centre with a radius of 800 pc × tan(0.16°) ∼ 2.2 pc estimated from the MAGIC data as shown in Table1. The calculation results are summarised in Table B.1. There is not a significant difference between the results obtained using these two different integration velocity ranges. We use 100 cm^{-3} and 200 cm^{-3} as a gas density for the head and tail regions for the modelling.

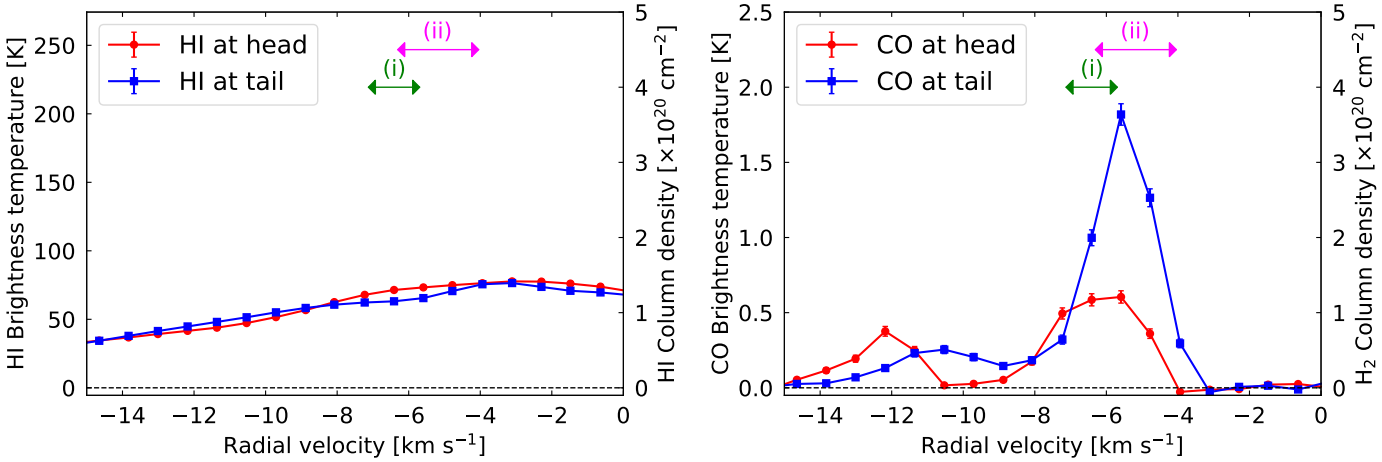

Fig. B.1. HI (left) and ^{12}CO ($J = 1 - 0$) (right) radial profile at the head and tail region. In both panels, red and blue data represent the profile of the head and tail regions. The green arrow labelled (i) show the velocity ranges pointed out by Kothes et al. (2001), while the magenta arrow labelled (ii) is those of Acciari et al. (2009) and Albert et al. (2020).